

Monte-Carlo Study of the (102°,90°) Physics Optics for LEP in 1998

John M. Jowett

15 April 1998

Abstract

In 1998 LEP will be run using an optics with phase advances $\mu_x = 102^\circ$ and $\mu_y = 90^\circ$ in the arc cells. This note summarises the main results from the optics evaluation procedure that is now routinely applied to new LEP optics. This includes the study of the orbits, optics and dynamic apertures of an ensemble of imperfect machines with corrections similar to those applied in operation. It provides predictions of performance and results of measurements that can be done when the optics is commissioned. A single SF sextupole family is used in order to provide a baseline for comparison of the effects of re-cabling the sextupoles. This will be treated in a subsequent note.

1 Introduction

To evaluate the potential performance of a new optics for LEP, it is necessary to perform calculations of orbits, optics, beam parameters and dynamic apertures on an ensemble of imperfect machines. Over the last few years, a standard procedure has evolved for this purpose. For the present note, it has been applied to a the "squeezed" (102°,90°) 1998 physics optics at 94 GeV. All SF sextupoles are excited with the same strength, corresponding to the situation that would have been obligatory if the SF sextupoles had not been recabled for the 1998 run. In fact, following the recabling of the SF sextupoles, other possibilities have been opened up. The improvement that these should bring will be treated in a follow-up note to this one.

The procedure followed is outlined in the note [1] which gave the corresponding results for the (102°,90°) tested in late 1997 at a lower energy. There is some additional discussion in [2]. To make it easy to compare (and for me to write), the results are presented in the same format although some explanatory text has been cut out. Many further results can be extracted from the database generated by the evaluation procedure which can be accessed via [4].

Full details of the configuration and the calculations can be found using the following information:

F05150B98v1.lep_odd, 102/90 for 1998 94 GeV

```
MAD working directory was:  
/afs/cern.ch/eng/lep/imperf/lep98/lm50usualSF  
Current directory: J:\lep98\imperf\lm50usualSF
```

2 Remarks on the results

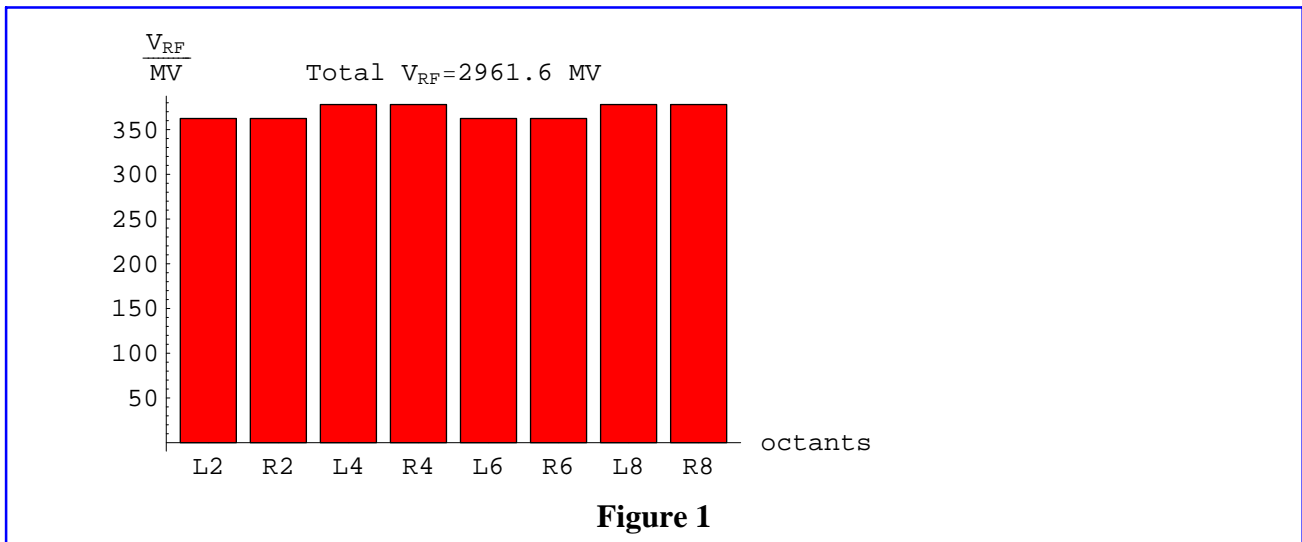
It was possible to find and correct the average closed orbit for all 30 machines. All machines remained stable when the solenoids and their pre-computed coupling compensation with tilted quadrupoles were switched on and when radiation was switched on.

In the following, the means, standard deviations and other statistical quantities refer to the distribution of quantities over the ensemble of 30 machines. The estimator for standard deviation quoted is always unbiased although it could be argued that a maximum-likelihood estimate (4% smaller here) would be justified for some physical quantities.

Because of the strong radiation effects, the orbit and optics are different for the two beams. Therefore many quantities are given for both electrons and positrons. Some quantities, such as the tune splits or centre-of-mass energies, have to be derived by combining properties of the two beams.

3 RF configuration

It was assumed, rather idealistically, that each superconducting RF unit provided a peak voltage of 42 MV and each copper one 2.2 MV and that all units were properly phased. The 1998 configuration resulted in the distribution of RF voltage by octant of LEP shown in Figure 1. The total voltage is more than the minimum necessary [6] for the beam energy.



4 Orbits and optics

The imperfections of each machine in the ensemble give rise to different closed orbits after correction. Furthermore, in a given machine, the positrons and electrons, despite seeing the same imperfections, move in opposite directions around the ring. Since the terms in their equations of motion describing synchrotron radiation are not time-reversal invariant, they have very different closed orbits (separated horizontally by several mm in some places). The optical functions codify the behaviour of small displacements from these closed orbit and these, too, will differ from machine to machine and from one beam to the other. This section summarises the statistical information on orbits, optical functions and derived quantities such as the separations at the interaction points (IPs).

4.1 Global optical parameters

Table 1 lists the statistics for a number of global quantities related to the optics. Some of these are derived from the traditional Courant-Snyder (labelled "CS" in the table) calculations and may not take proper account of the radiation and RF effects but still have some indicative value. The tunes quoted are the correct tunes on the 6-dimensional closed orbit.

Quantity	Symbol	Mean	σ_{est}	Units
Momentum compaction for e^+	α_c^+	0.0001559	2.25×10^{-8}	
Momentum compaction for e^-	α_c^-	0.0001559	2.24×10^{-8}	
Max. horizontal CS β -function for e^+	$\beta_x^{\text{max}+}$	526.3	22.9	m
Max. horizontal CS β -function for e^-	$\beta_x^{\text{max}-}$	524.6	17.8	m
Max. vertical CS β -function for e^+	$\beta_y^{\text{max}+}$	433.9	3.69	m
Max. vertical CS β -function for e^-	$\beta_y^{\text{max}-}$	434.6	3.53	m
Horizontal tune for e^+	Q_1^+	0.2839	0.0000275	
Horizontal tune for e^-	Q_1^-	0.2841	0.00251	
Vertical tune for e^+	Q_2^+	0.1949	0.0000281	
Vertical tune for e^-	Q_2^-	0.2154	0.111	
Synchrotron tune for e^+	Q_3^+	0.1249	0.0000318	
Synchrotron tune for e^-	Q_3^-	0.1249	0.00003	
Horizontal tune split	ΔQ_1^\pm	-0.0002365	0.0025	
Vertical tune split	ΔQ_2^\pm	-0.0205	0.111	
Horizontal CS chromaticity for e^+	$Q_x'^+$	1.021	0.342	
Horizontal CS chromaticity for e^-	$Q_x'^-$	0.8768	0.397	
Vertical CS chromaticity for e^+	$Q_y'^+$	0.4902	0.126	
Vertical CS chromaticity for e^-	$Q_y'^-$	0.4664	0.138	
Horizontal chromaticity split	$\Delta Q_x'^\pm$	0.144	0.163	
Vertical chromaticity split	$\Delta Q_y'^\pm$	0.02377	0.0775	

Table 1

Since the tune correction for each machine was done on the positrons, the tunes of the positron beams have a very small spread while the electrons are left with a certain spread. The vertical tune-split is relatively small, thanks to the fairly symmetric RF voltage distribution.

4.2 Global orbits

Table 2 gives some global orbit parameters, where notations like $\overline{x^2}$ denote averages around the ring. The *average* e^+e^- orbit was corrected to 0.6 and 0.4 mm RMS in the horizontal and vertical planes. The larger RMS values for individual beams in the horizontal plane reflect the energy-sawtoothing.

Quantity	Symbol	Mean	σ_{est}	Units
RMS horizontal orbit for e^+	$\sqrt{\overline{x^2}}^+$	1.4	0.0413	mm
RMS horizontal orbit for e^-	$\sqrt{\overline{x^2}}^-$	1.4	0.0404	mm
Max. horizontal orbit for e^+	x_{max}^+	6.164	0.679	mm
Max. horizontal orbit for e^-	x_{max}^-	6.18	0.752	mm
RMS vertical orbit for e^+	$\sqrt{\overline{y^2}}^+$	0.3514	0.017	mm
RMS vertical orbit for e^-	$\sqrt{\overline{y^2}}^-$	0.3556	0.0272	mm
Max. vertical orbit for e^+	y_{max}^+	1.508	0.33	mm
Max. vertical orbit for e^-	y_{max}^-	1.526	0.343	mm

Table 2

4.3 Orbits and separations at the interaction points

More detailed information about the orbits at the interaction points is given in Table 3.

Quantity		Mean	$\sigma(\text{est})$	Units
Horizontal orbit for e ⁺ [IP2]	x(IP2) ⁺	-0.02423	0.21	mm
Horizontal orbit for e ⁻ [IP2]	x(IP2) ⁻	-0.00462	0.204	mm
Horizontal orbit for e ⁺ [IP4]	x(IP4) ⁺	0.00116	0.185	mm
Horizontal orbit for e ⁻ [IP4]	x(IP4) ⁻	-0.01826	0.189	mm
Horizontal orbit for e ⁺ [IP6]	x(IP6) ⁺	-0.05864	0.208	mm
Horizontal orbit for e ⁻ [IP6]	x(IP6) ⁻	-0.03692	0.199	mm
Horizontal orbit for e ⁺ [IP8]	x(IP8) ⁺	0.01158	0.16	mm
Horizontal orbit for e ⁻ [IP8]	x(IP8) ⁻	-0.007389	0.16	mm
Horizontal separation [IP2]	Δx^{\pm} [IP2]	-0.01961	0.0379	mm
Horizontal separation [IP4]	Δx^{\pm} [IP4]	0.01942	0.0339	mm
Horizontal separation [IP6]	Δx^{\pm} [IP6]	-0.02172	0.038	mm
Horizontal separation [IP8]	Δx^{\pm} [IP8]	0.01897	0.0408	mm
Vertical orbit for e ⁺ [IP2]	y(IP2) ⁺	-0.004505	0.125	mm
Vertical orbit for e ⁻ [IP2]	y(IP2) ⁻	-0.004963	0.125	mm
Vertical orbit for e ⁺ [IP4]	y(IP4) ⁺	-0.03824	0.116	mm
Vertical orbit for e ⁻ [IP4]	y(IP4) ⁻	-0.0387	0.116	mm
Vertical orbit for e ⁺ [IP6]	y(IP6) ⁺	-0.01673	0.116	mm
Vertical orbit for e ⁻ [IP6]	y(IP6) ⁻	-0.01713	0.117	mm
Vertical orbit for e ⁺ [IP8]	y(IP8) ⁺	0.04041	0.127	mm
Vertical orbit for e ⁻ [IP8]	y(IP8) ⁻	0.04025	0.127	mm
Vertical separation [IP2]	Δy^{\pm} [IP2]	0.0004583	0.00147	mm
Vertical separation [IP4]	Δy^{\pm} [IP4]	0.0004594	0.00183	mm
Vertical separation [IP6]	Δy^{\pm} [IP6]	0.0004084	0.00162	mm
Vertical separation [IP8]	Δy^{\pm} [IP8]	0.0001583	0.00192	mm

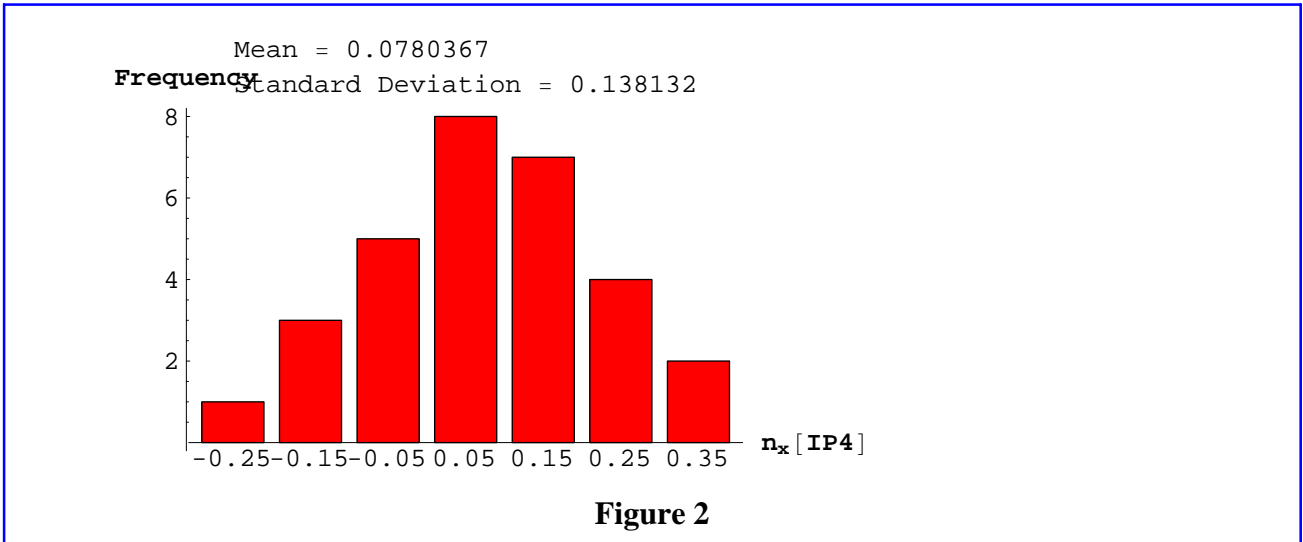
Table 3

As usual in LEP, there are small horizontal and vertical separations at the interactions points. In operation the essentially random (zero mean) vertical separations are usually removed with electrostatic separators. No separators are available in the horizontal plane. However if we express the separation in units of the beam size,

$$n_x \simeq \frac{\Delta x^{\pm}}{\sqrt{\beta_{x1^+} \varepsilon_{1^+}}}, n_y \simeq \frac{\Delta y^{\pm}}{\sqrt{\beta_{x1^+} \varepsilon_{1^+}}} \quad (1)$$

The largest horizontal separations actually occur in IP4 and are distributed according to the histogram in Figure 2.

It is clear that these are not worth correcting when compared with the beam size. They may however increase if RF units trip [8].



4.4 Optical functions at the interaction points

Table 4 gives the statistics for the β -functions in the interaction points (the values for the ideal machine being $\beta_x^* = 1.5$ m, $\beta_y^* = 0.05$ m). Each machine in the ensemble has had its vertical β -function corrected by a procedure that mimics the one followed in operation. The values for the imperfect machine are "measured" after orbit correction. A matching calculation is carried out using the ideal machine model to find increments of the QSO quadrupoles that would produce these values. The negatives of these increments are then applied to the quadrupoles.

Quantity		Mean	σ (est)	Units
Horizontal β -function for e ⁺ [IP2]	$\beta_{x1}(\text{IP2})^+$	1.484	0.0732	m
Horizontal β -function for e ⁻ [IP2]	$\beta_{x1}(\text{IP2})^-$	1.494	0.0782	m
Horizontal β -function for e ⁺ [IP4]	$\beta_{x1}(\text{IP4})^+$	1.491	0.0705	m
Horizontal β -function for e ⁻ [IP4]	$\beta_{x1}(\text{IP4})^-$	1.51	0.075	m
Horizontal β -function for e ⁺ [IP6]	$\beta_{x1}(\text{IP6})^+$	1.501	0.073	m
Horizontal β -function for e ⁻ [IP6]	$\beta_{x1}(\text{IP6})^-$	1.487	0.0701	m
Horizontal β -function for e ⁺ [IP8]	$\beta_{x1}(\text{IP8})^+$	1.486	0.0663	m
Horizontal β -function for e ⁻ [IP8]	$\beta_{x1}(\text{IP8})^-$	1.475	0.0731	m
Vertical β -function for e ⁺ [IP2]	$\beta_{y2}(\text{IP2})^+$	0.04989	0.000404	m
Vertical β -function for e ⁻ [IP2]	$\beta_{y2}(\text{IP2})^-$	0.05004	0.000649	m
Vertical β -function for e ⁺ [IP4]	$\beta_{y2}(\text{IP4})^+$	0.05002	0.0004	m
Vertical β -function for e ⁻ [IP4]	$\beta_{y2}(\text{IP4})^-$	0.04995	0.000779	m
Vertical β -function for e ⁺ [IP6]	$\beta_{y2}(\text{IP6})^+$	0.04994	0.000444	m
Vertical β -function for e ⁻ [IP6]	$\beta_{y2}(\text{IP6})^-$	0.04988	0.000707	m
Vertical β -function for e ⁺ [IP8]	$\beta_{y2}(\text{IP8})^+$	0.04989	0.000399	m
Vertical β -function for e ⁻ [IP8]	$\beta_{y2}(\text{IP8})^-$	0.0498	0.00085	m

Table 4

In the note [1], a small error crept into the procedure: IP8 was corrected on the basis of the values measured in IP6. This bug was corrected for the present study so the points are much more closely

clustered around 0.05 m. The following Figure 3 shows the resulting correlations of vertical β -functions between beams in each IP. The coordinates of each point are given by the β -functions of the positron and electron. The four clouds of points represent the values at each IP.

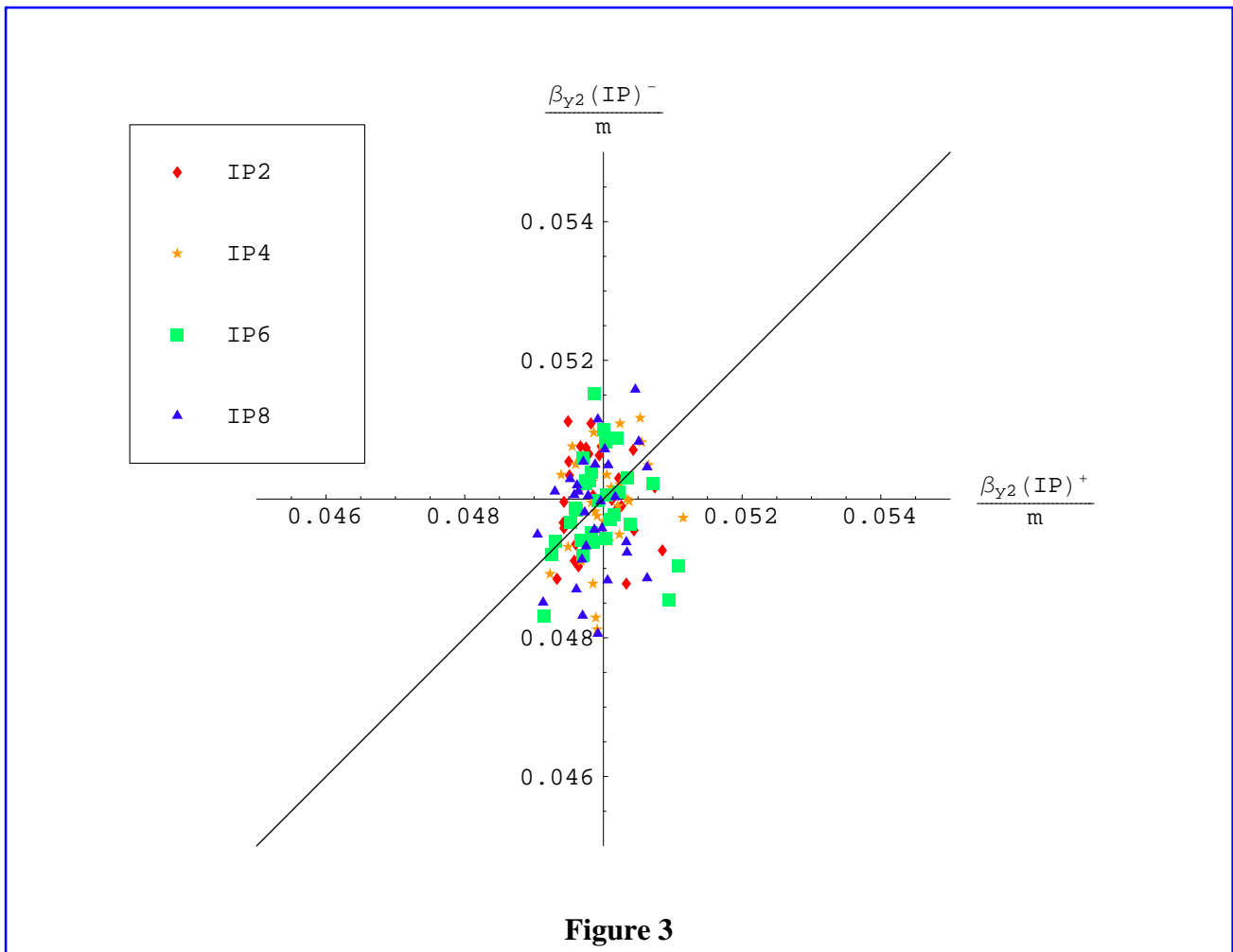


Figure 3

5 Parameters of the beams

As a further consequence of the different orbits and optics among machines and between beams in a given machine, beam parameters determined by integrals along the 6-dimensional closed orbit can differ. This section summarises the statistical information for some of the most important beam parameters.

5.1 Energy loss and radiation damping

Table 5 is a summary of the values of selected parameters related to the energy lost by synchrotron radiation and the radiation damping. The energy lost per turn is slightly higher than the 2282.5 MeV given by the standard calculation [6,7] using synchrotron radiation integrals for a particle with constant nominal energy on the central trajectory passing through the centres of the elements. The additional 2-3 MeV of energy is lost as the closed orbit passes off-centre through quadrupoles and other elements because of energy sawtoothing and the imperfections.

The damping partition numbers are close to their nominal values, except in the vertical mode. The correlation plot between damping partition numbers for the two beams is shown in Figure 4.

Quantity	Symbol	Mean	σ (est)	Units
Beam energy for e^+	E_b^+	94.	0.	GeV
Beam energy for e^-	E_b^-	94.	0.	GeV
Average momentum deviation for e^+	δ_s^+	0.	0.	
Average momentum deviation for e^-	δ_s^-	0.	0.	
Energy loss per turn for e^+	U_0^+	2285.	0.33	MeV
Energy loss per turn for e^-	U_0^-	2285.	0.389	MeV
Horizontal damping partition for e^+	J_1^+	1.008	0.0199	
Horizontal damping partition for e^-	J_1^-	1.008	0.0187	
Vertical damping partition for e^+	J_2^+	0.9734	0.0736	
Vertical damping partition for e^-	J_2^-	0.9744	0.0888	
Longitudinal damping partition for e^+	J_3^+	2.018	0.0752	
Longitudinal damping partition for e^-	J_3^-	2.018	0.0882	
Horizontal damping time for e^+	τ_1^+	0.007259	0.000142	sec
Hor. damping time in turns for e^+	τ_{1+}/T_0^+	81.63	1.6	
Vertical damping time for e^+	τ_2^+	0.007566	0.000684	sec
Vert. damping time in turns for e^+	τ_{2+}/T_0^+	85.09	7.69	
Longitudinal damping time for e^+	τ_3^+	0.00363	0.000127	sec
Long. damping time in turns for e^+	τ_{3+}/T_0^+	40.82	1.43	

Table 5

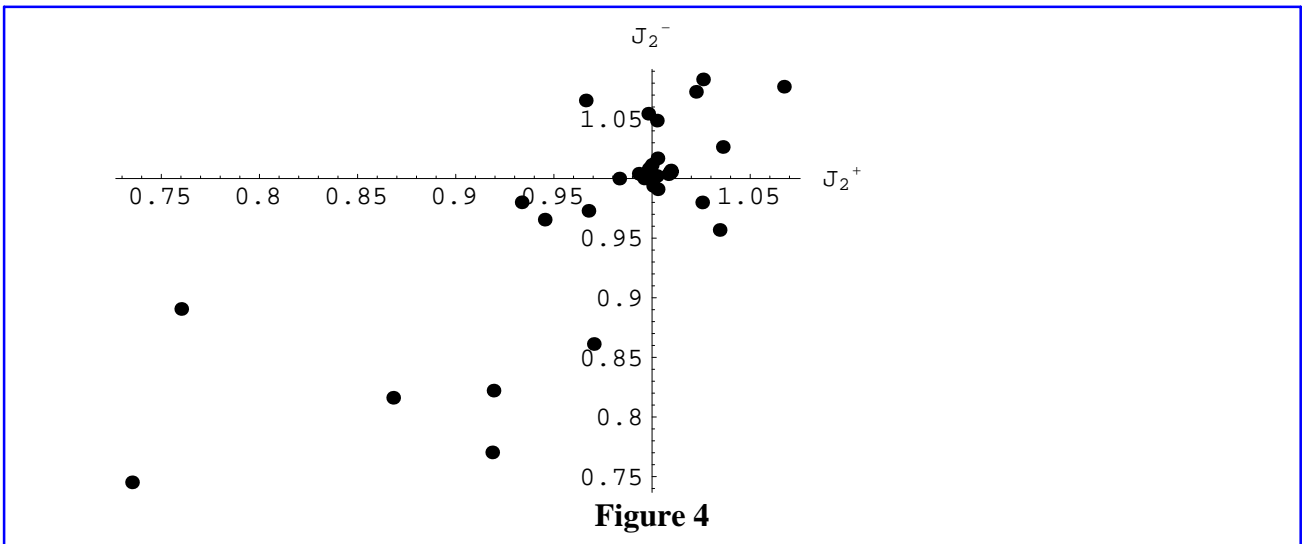


Figure 4

It can be seen from the Figure 5 that, there is a non-linear correlation between the shift in the damping partition number and the RMS vertical dispersion around the ring. The change can be produced in strong quadrupoles where there is a combination of vertical orbit *and* dispersion.

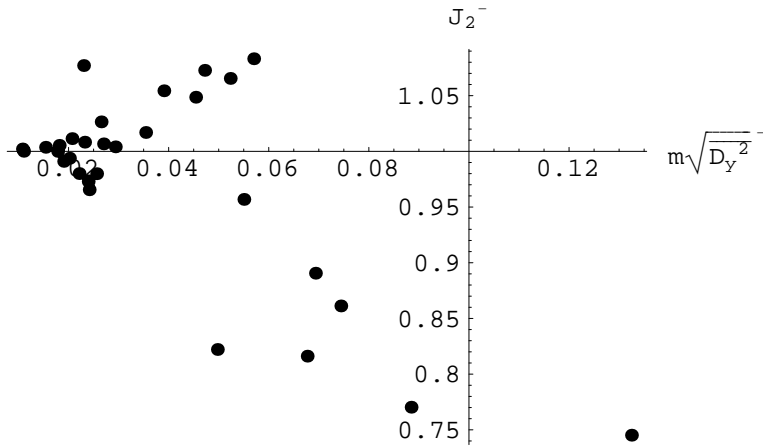


Figure 5

5.2 Centre-of-mass energy in collision

Knowing the values of the canonical momenta p_t^+ , p_t^- (as defined by MAD Version 8 [3]) on the closed orbits of the two beams, and neglecting terms involving the mass of the electron, the centre-of-mass (CM) energy in collisions is given by

$$w = 2 \left(E_0^+ E_0^- (p_t^- + 1) (p_t^+ + 1) + \sqrt{(E_0^-)^2 (p_t^- + 1)^2 - m_e^2} \sqrt{(E_0^+)^2 (p_t^+ + 1)^2 - m_e^2} \right)^2 + 2 m_e^2 \quad (2)$$

$$\approx 4 E_0^+ E_0^- (p_t^- + 1) (p_t^+ + 1) - (E_0^+ / E_0^- - E_0^- / E_0^+) m_e^2$$

where the second form includes terms up to second order in the small quantities $\frac{m_e}{E_0}, p_t^-, p_t^+$. Usually the nominal beam energies are equal and the approximate form simplifies to:

$$w = 4 E_0^2 (p_t^- + 1) (p_t^+ + 1) \quad (3)$$

but we shall always use the exact form in the following.

At IP2 for example, the prepared ensemble of imperfect machines has a distribution of CM energies. This can be expressed as a deviation in MeV from the nominal 188 GeV as in Figure 6.

Imperfections in the present Monte-Carlo simulations indicate possible drifts of machine conditions over an operating period due to the effects included. They do not include other external trends in the machine conditions. With these caveats, the expected variation is of the order of 5 MeV.

The CM energies may differ from one experiment to another, mainly because of the RF voltage distribution. The 4 data sets in Figure 7 are the shift in CM energies at each IP. To make the plot clearer, the machines have been sorted according to the CM energy in IP6. The horizontal axis is just the resulting indexing of the machines.

The correlations in the ensemble of prepared machines are clear from this plot.

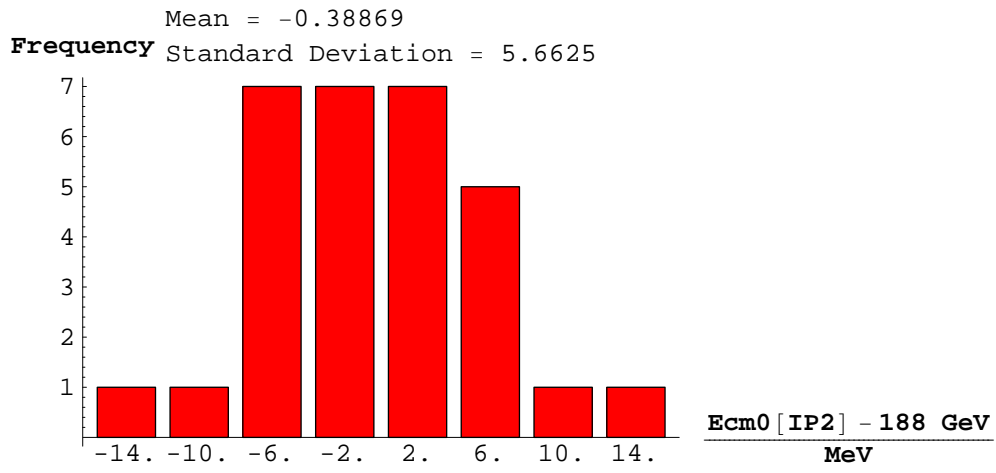


Figure 6

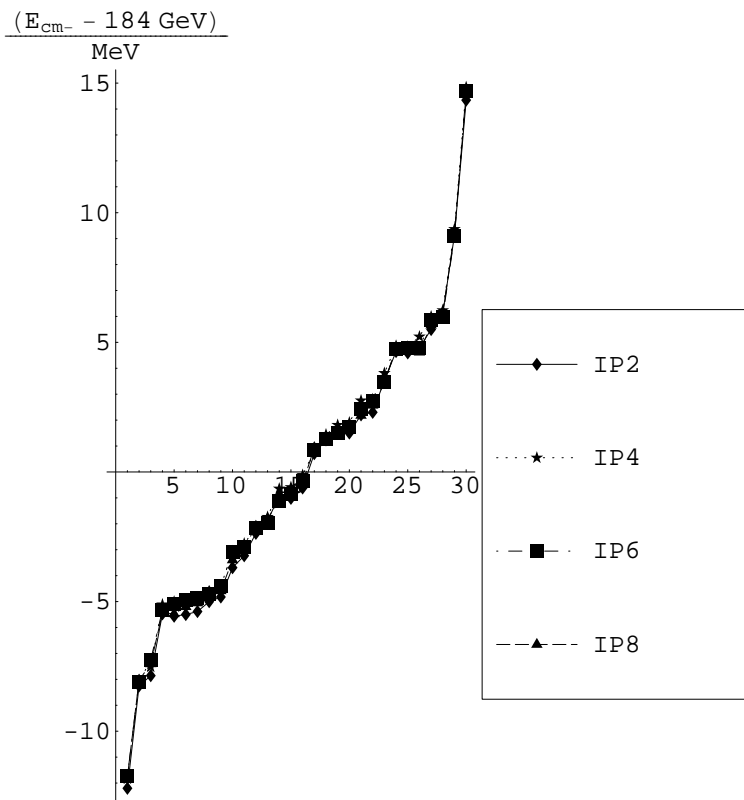


Figure 7

5.3 Emittances and energy spread

Table 6 summarises the distributions of the emittances and related quantities. The horizontal emittance has a rather small spread about its nominal value.

Quantity	Symbol	Mean	σ (est)	Units
Horizontal emittance for e^+	ε_1^+	40.5	1.49	nm
Horizontal emittance for e^-	ε_1^-	40.44	1.01	nm
Vertical emittance for e^+	ε_2^+	0.8131	1.25	nm
Vertical emittance for e^-	ε_2^-	0.8884	1.46	nm
Fractional energy spread for e^+	σ_ε^+	0.001471	0.0000261	
Fractional energy spread for e^-	σ_ε^-	0.001472	0.0000311	
Bunch length for e^+ [IP2]	$\sigma_z(\text{IP2})^+$	0.007795	0.000138	m

Table 6

The emittance ε_2 of the mainly-vertical mode is critical for the performance of the machine. The present simulation includes most optical effects that generate it (except the electrostatic separation bumps) but it should be kept in mind that the emittances given in Table 6 are the result of a *linear* eigenvector calculation. Roughly speaking, the linear vertical emittance has two components:

- The vertical emittance generated by linear coupling. This includes the transverse betatron coupling generated by solenoids and skew-quadrupole fields and the linear synchro-betatron coupling generated by dispersion at RF cavities.
- The intrinsic vertical emittance generated by quantum excitation in locations where there is a magnetic field and a non-zero value of the optical function β_{y3} (or "dispersion"). The contribution of this effect to the emittance is inversely proportional to the vertical damping rate.

It has been shown [2] that the true vertical emittance may be larger than given by the linear calculation because of nonlinear effects. Quantum tracking results are not reported here.

Apart from a single outlying machine in the ensemble, the emittances of the positrons and electrons are rather well-matched (see Figure 8, in which the solid line is the diagonal $x = y$, not a fit).

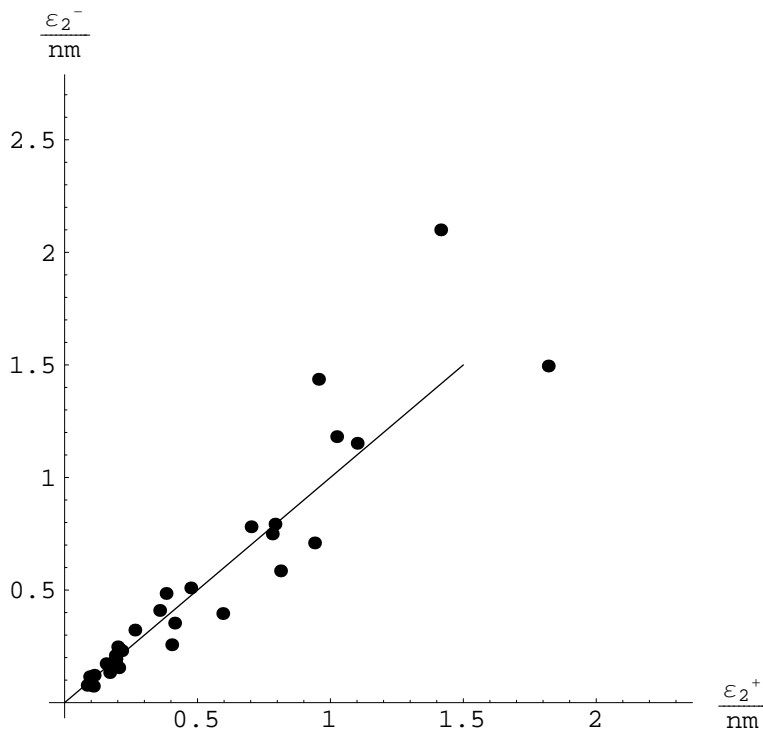


Figure 8

Since $\epsilon_2 \propto \langle D_y^2 \rangle / J_2$, one would expect that some part of the distribution of vertical emittances can be attributed to the variation of the damping partition number of the mainly-vertical mode between machines (see Figure 4). However both the vertical quantum excitation and the damping partition depend on the vertical dispersion function. A plot of the vertical emittance against the RMS vertical dispersion, Figure 9, suggests a power-law behaviour

$$\epsilon_2 \propto \overline{\langle D_y^2 \rangle}^{p/2}. \tag{4}$$

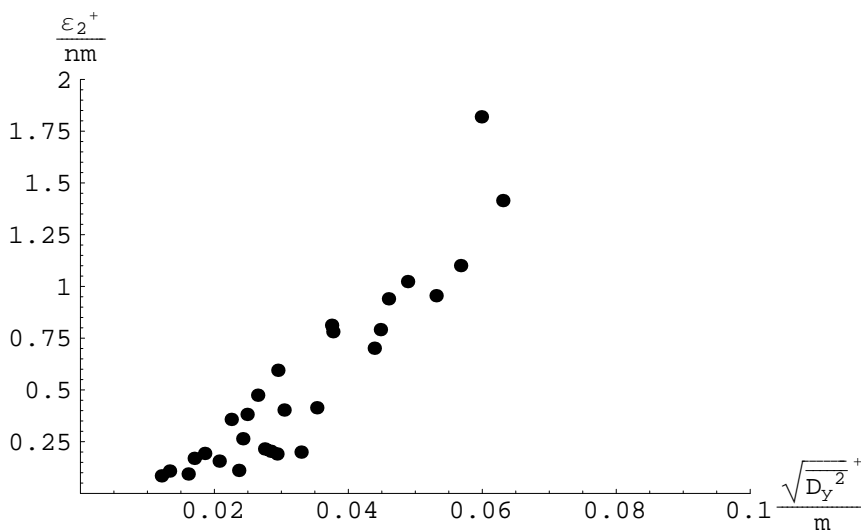


Figure 9

To extract the power p , which we expect to be somewhat larger than 2, we can plot the Pearson correlation, r_p , between the left and right-hand sides of (4) as a function of p . The two curves in the following figure are obtained from the positron and electron data.

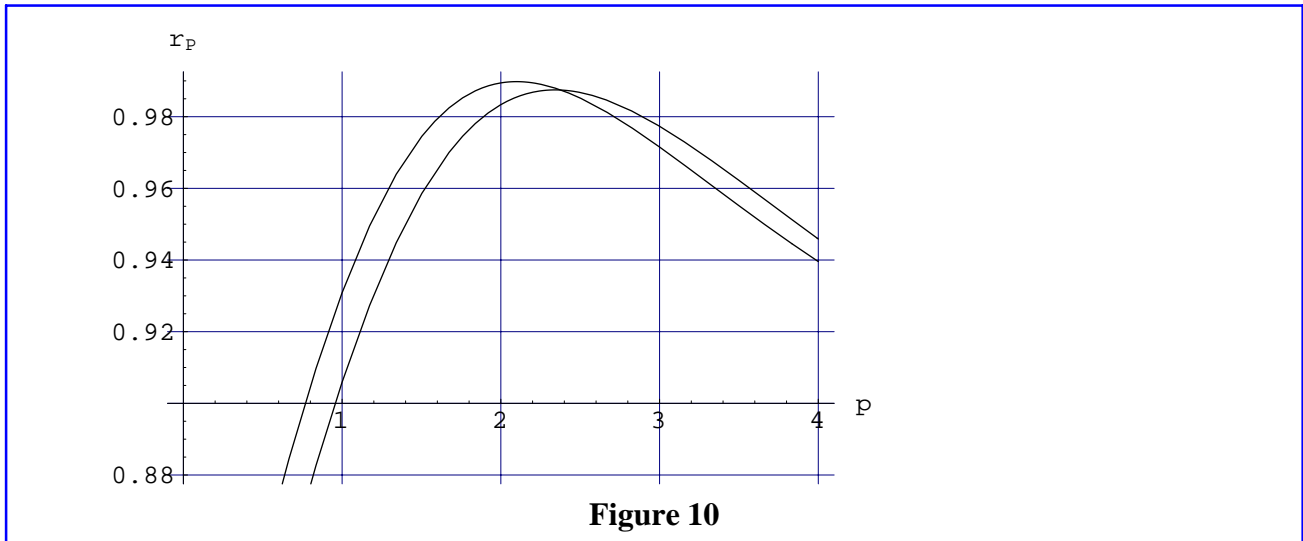


Figure 10

The maxima of the two curves occur at

$$\{2.09942, 2.34226\}$$

$$p = 2.09942 \quad \text{and} \quad p = 2.34226 \quad (5)$$

and, taking the average of these two values, we can postulate an empirical formula for the vertical emittance in terms of the RMS vertical dispersion. A fit including a constant term to take account of residual betatron coupling gives

$$\frac{\varepsilon_2}{\text{nm}} = 728.031 \left(\frac{D_y^{\text{rms}}}{m} \right)^{2.22} + 0.0815727$$

and this is plotted, together with the data for both beams ("*" for e^+) in Figure 11. This formula is to be interpreted in a statistical sense. It may well be that the vertical emittance is particularly sensitive to the values of the vertical dispersion function in certain locations.

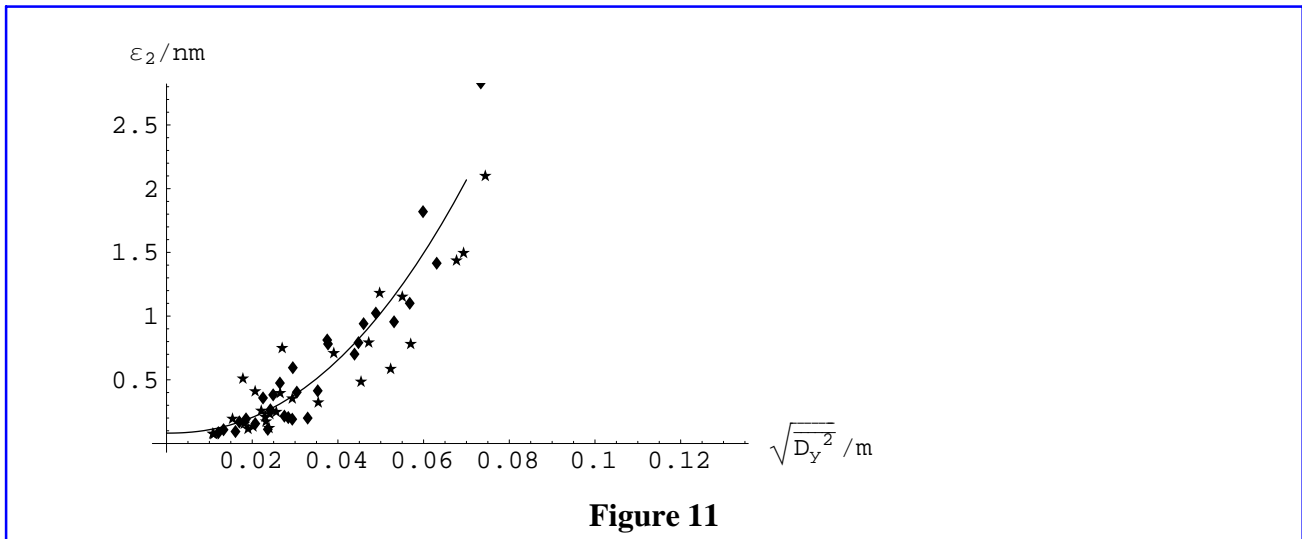


Figure 11

The numerical coefficient in the fit is appropriate for an RMS vertical dispersion measured all around the ring - the numerical coefficient will be different for an average restricted to the pickups.

6 Dynamic Aperture

The transverse dynamic apertures A_x, A_y are defined as the largest stable initial values of the "Courant-Snyder invariants". Although not invariants, these are just twice the action variables of the first two eigenmodes of linear oscillation (roughly speaking, the "horizontal and vertical betatron motion") about the 6-dimensional closed orbit and are expressed in metres. The emittances are the averages of the actions over the beam distribution. The projection of the dynamic aperture of the third mode ("synchrotron motion") is entirely analogous but is customarily converted to a dimensionless form in which its square root can be interpreted as the amplitude of a fractional momentum deviation in percent.

In LEP, it is convenient and has become customary to quote the *square roots* of the dynamic aperture projections rather than the quantities themselves.

The following summary table shows that this optics has a large dynamic aperture in the mainly-horizontal mode:

Quantity		Mean	$\sigma(\text{est})$
Horizontal dynamic aperture	$10^3 \sqrt{A_x} / m$	2.391	0.147
Vertical dynamic aperture	$10^3 \sqrt{A_y} / m$	1.188	0.0858
Longitudinal dynamic aperture	$\sqrt{A_t} / \%$	1.5	0.107

Table 7

This confirms that the longitudinal dynamic aperture is indeed given by the RF voltage. That is, the chromaticity correction is adequate.

It is worth recalling here that, in order to evaluate the momentum acceptance correctly, it is essential to track particles with initial synchrotron phases scanned over the interval $[0, 2\pi)$. Failure to do this in the case of LEP can result in a momentum acceptance up to a factor of 2 too large. This is illustrated in Figure 12, a survival plot of particles tracked in the plane $A_y = 0$ for one particular machine in the

ensemble. Black dots represent initial conditions of particles that survived to the end of the tracking (100 turns) and progressively lightening shades of grey indicate shorter survival times (of course this is better seen in colour). It is only when all phases are tracked that the true momentum acceptance is found.

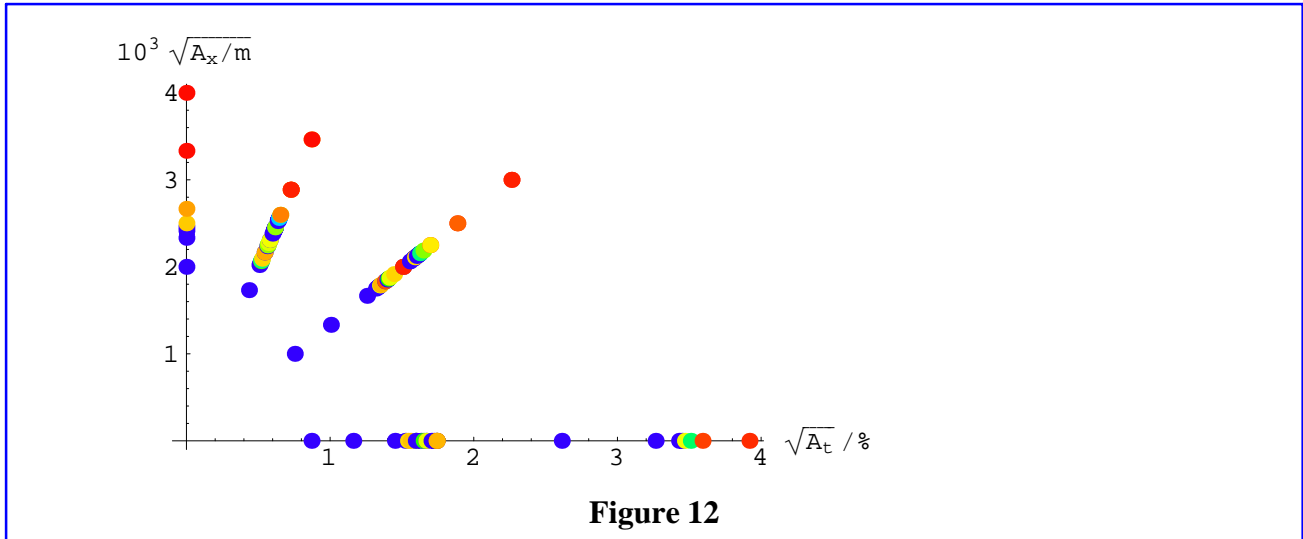


Figure 13 shows the survival plot in the particle amplitude space. In both these plots, the synchrotron phase dimension is "rolled-up" so that several points of varying synchrotron phase can be on top of each other. The number of particles tracked for this machine is 421.

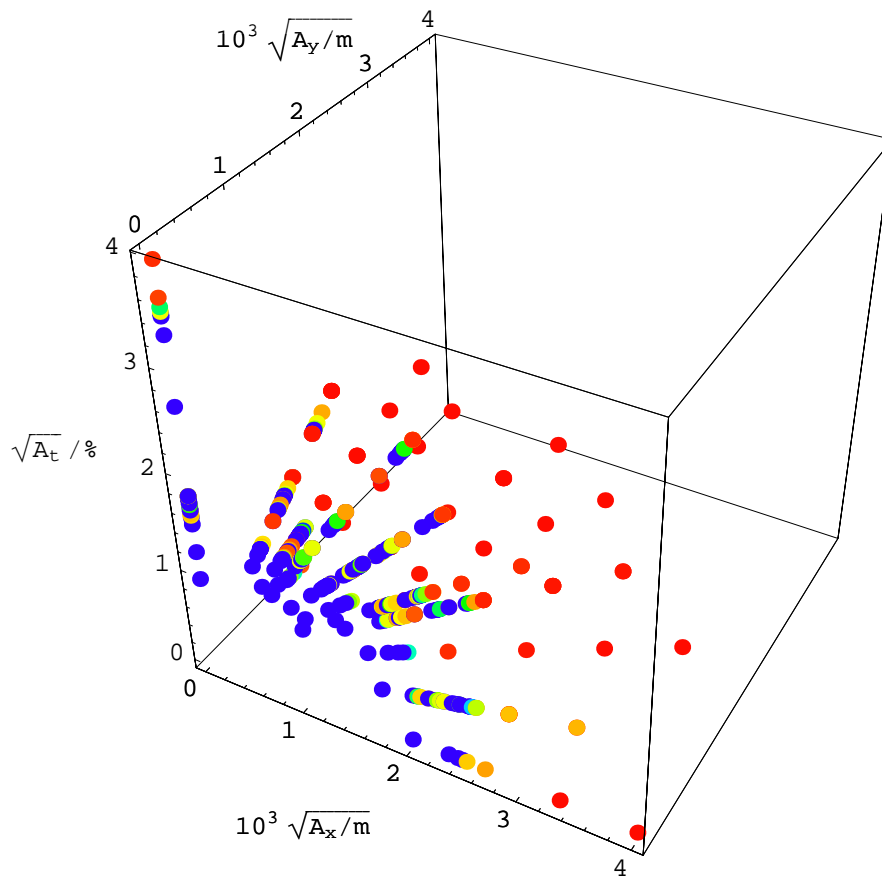
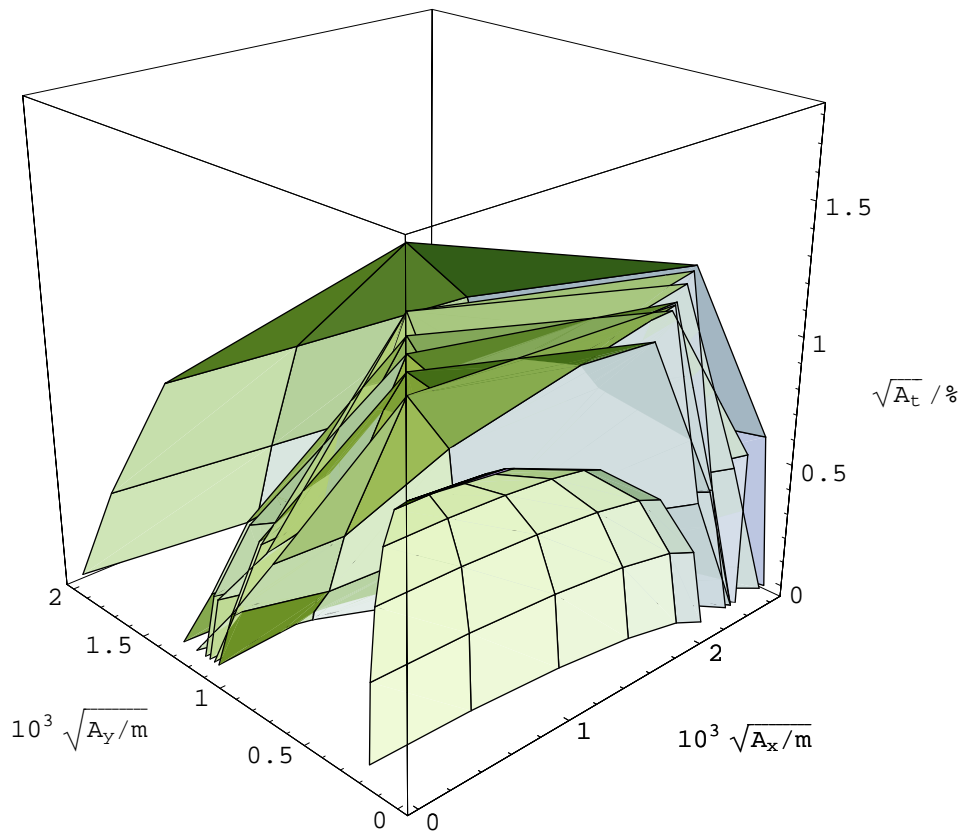


Figure 13

Figure 14 provides a graphical impression of the distribution of the 4D dynamic aperture surfaces projected into the space of amplitudes of the three normal modes. To avoid cluttering the figure too much, only the first 8 of the 27 dynamic apertures are shown. However they are quite representative of the full ensemble. The outermost surface is the dynamic aperture of the perfect machine. The inner ellipsoidal surface has projections on the axes corresponding to $(10\sigma_1, 10\sigma_2, 7\sigma_3)$ derived from the linear emittances. It is shown purely to indicate the scale of the dynamic aperture and plays no role in the calculation. The surface shown actually corresponds to the beam parameters of the third machine in the ensemble which happens to have $\varepsilon_2^+ = 0.58$ nm.

**Figure 14**

We can also plot the correlations of the intersections of these surfaces with pairs of axes. For comparison, a point representing the ideal machine is included.

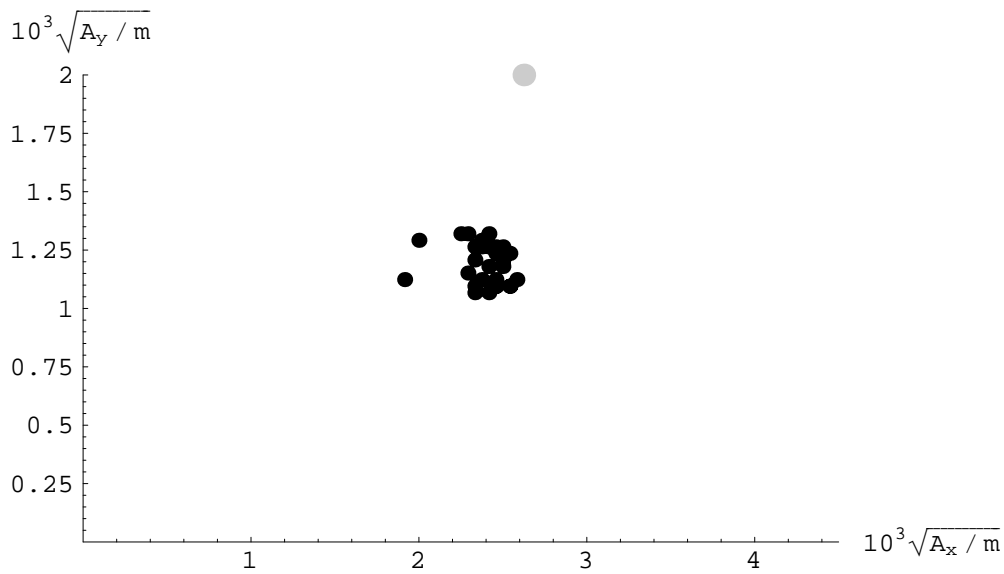


Figure 15

There is no particular correlation between the horizontal dynamic aperture and the momentum acceptance (Figure 16). Indeed further exploration of the database of imperfect machines reveals no particular correlations of dynamic aperture components with quantities such as the emittances, dispersions, tunes or chromaticities.

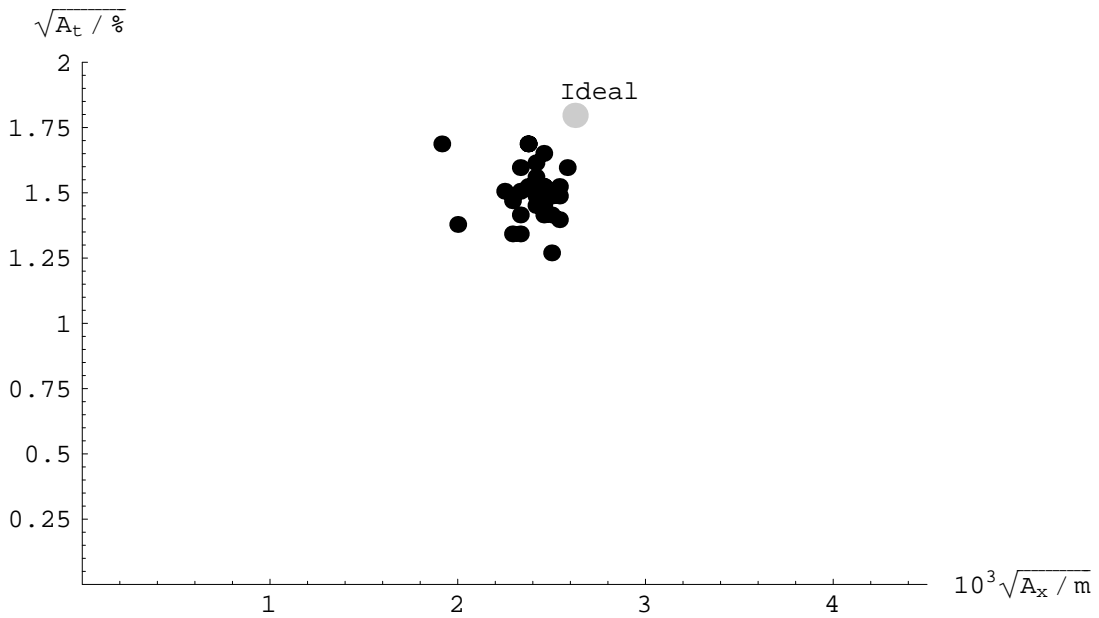


Figure 16

7 Conclusions

The 1998 LEP optics with $\mu_x = 102^\circ$ and $\mu_y = 90^\circ$ in the arc cells can be expected to perform well at 94 GeV once the usual corrections are applied (even with a single SF sextupole family). The dynamic aperture appears large enough and the vertical emittance can be made small. As in all other LEP optics studied [2], the dominant component of the linear vertical emittance is generated by vertical quantum excitation since the linear betatron coupling is straightforwardly eliminated.

These computations can be taken as predictions for the performance of the optics, *once it is well run-in* at 94 GeV. In particular, the dynamic aperture is to be compared with measurement (kick measurements or properly interpreted measurements using collimators). These results may not apply at 45 GeV.

The physical mechanisms determining the dynamic aperture and the possibility of enhanced beam tails will be discussed in a forthcoming note on the effects of recabling the sextupoles. One of the main purposes of this note was to provide a baseline for this comparison.

7.1 Acknowledgements

Thanks to Malika Meddahi for providing the optics files.

8 References

- [1] J.M. Jowett, *Monte-Carlo Study of the (102°,90°) Physics Optics for LEP*, CERN SL Note 97-84 (AP), and <http://wwwslap.cern.ch/~jowett/lep97/mu10290by5A/SLNote97-84.html>
- [2] J.M. Jowett, *Vertical Beamsize (and other calculations) in Various Optics*, in Proc. 8th LEP Performance, Chamonix, January 1998, CERN-SL-98-006 (1998)
http://www.cern.ch/CERN/Divisions/SL/publications/chamx98/PAPERS/JJ3_032.PDF
- [3] Hans Grote, F. Christoph Iselin, *The MAD Program, User's Reference Manual*, CERN/SL/90-13 (AP), and <http://wwwslap.cern.ch/~fci/mad/mad.html>
- [4] <http://wwwslap.cern.ch/~jowett/JMJdocs.html>
- [5] J.M. Jowett, *Dynamic Aperture for LEP: physics and calculations*, in J. Poole (Ed.), Proc. 4th LEP Performance Workshop, CERN SL/94-06 (DI).
Comparisons have been made with well-known formulas [7] that neglect the effects of energy-sawtoothing and imperfections on the orbit and optics. A set of results roughly corresponding to the conditions of the present simulations can be found at
- [6] <http://wwwslap.cern.ch/~jowett/lep97/mu10290/mu10290by5A.wigout>
- [7] M. Sands, *The Physics of Electron Storage Rings*, SLAC-121 (1970).
- [8] J.M. Jowett, *Effects of an RF Trip in a Perfect LEP2*, CERN LEP2 Note 94-17 (1994).